

SCIENTIFIC REPORTS



OPEN

Calculation of π and Classification of Self-avoiding Lattices via DNA Configuration

Anshula Tandon¹, Seungjae Kim¹, Yongwoo Song¹, Hyunjae Cho¹, Saima Bashar¹, Jihoon Shin², Tai Hwan Ha^{ID 2,3} & Sung Ha Park^{ID 1}

Numerical simulation (*e.g.* Monte Carlo simulation) is an efficient computational algorithm establishing an integral part in science to understand complex physical and biological phenomena related with stochastic problems. Aside from the typical numerical simulation applications, studies calculating numerical constants in mathematics, and estimation of growth behavior via a non-conventional self-assembly in connection with DNA nanotechnology, open a novel perspective to DNA related to computational physics. Here, a method to calculate the numerical value of π , and way to evaluate possible paths of self-avoiding walk with the aid of Monte Carlo simulation, are addressed. Additionally, experimentally obtained variation of the π as functions of DNA concentration and the total number of trials, and the behaviour of self-avoiding random DNA lattice growth evaluated through number of growth steps, are discussed. From observing experimental calculations of π (π_{exp}) obtained by double crossover DNA lattices and DNA rings, fluctuation of π_{exp} tends to decrease as either DNA concentration or the number of trials increases. Based upon experimental data of self-avoiding random lattices grown by the three-point star DNA motifs, various lattice configurations are examined and analyzed. This new kind of study inculcates a novel perspective for DNA nanostructures related to computational physics and provides clues to solve analytically intractable problems.

A multitude of analytically intractable problems in various disciplines are addressed by performing numerical simulations that employ a computational model of a system to describe its complex behaviour over a time period by incorporating given variables. One such commonly used model is Monte Carlo (MC) simulation¹ that refers to an effective computational algorithm adopted to perform an underlying stochastic and random sampling experiment on a computer to calculate various outcomes. MC simulation is used in science and engineering to understand complex physical phenomena, generate useful mathematical functions, and predict complicated algorithmic processes. Interestingly, the MC method has also been effectively used to understand complex biological process mechanisms such as the biological self-assembly behaviour, biomolecule dynamics, and the interaction between biomolecules and nanomaterials^{2–23}.

Among typical MC simulation applications, there are two interesting ones; calculating π (one of most important mathematical constants defined as the ratio of a circle's circumference to its diameter), and interpreting a self-avoiding walk (an abstract model describing the behaviour of chain like entities where no two points can occupy the same place)²⁴. Several approaches have been adapted to calculate π , among which the famously used one is Buffon's needle approach²⁵. The MC method is also used to enumerate the characteristics of the self-avoiding walk, to interpret the possibility to estimate proper paths.

The fabrication of various dimensional DNA nanostructures is well established due to the programmability of DNA base sequences and the stability of DNA molecules. Although these artificially designed DNA nanostructures find various applications as physical, chemical, or biomedical devices and sensors^{26–32}, calculating mathematical constants and incorporating abstract modeling via DNA nanostructures are rarely discussed.

¹Department of Physics and Sungkyunkwan Advanced Institute of Nanotechnology (SAINT), Sungkyunkwan University, Suwon, 16419, Korea. ²Hazards Monitoring BNT Research Center, Korea Research Institute of Bioscience and Biotechnology (KRIBB), Daejeon, 34141, Korea. ³Department of Nanobiotechnology, KRIBB School of Biotechnology, Korea University of Science and Technology (UST), Daejeon, 34113, Korea. Anshula Tandon and Seungjae Kim contributed equally. Correspondence and requests for materials should be addressed to T.H.H. (email: taihan@kribb.re.kr) or S.H.P. (email: sunghapark@skku.edu)

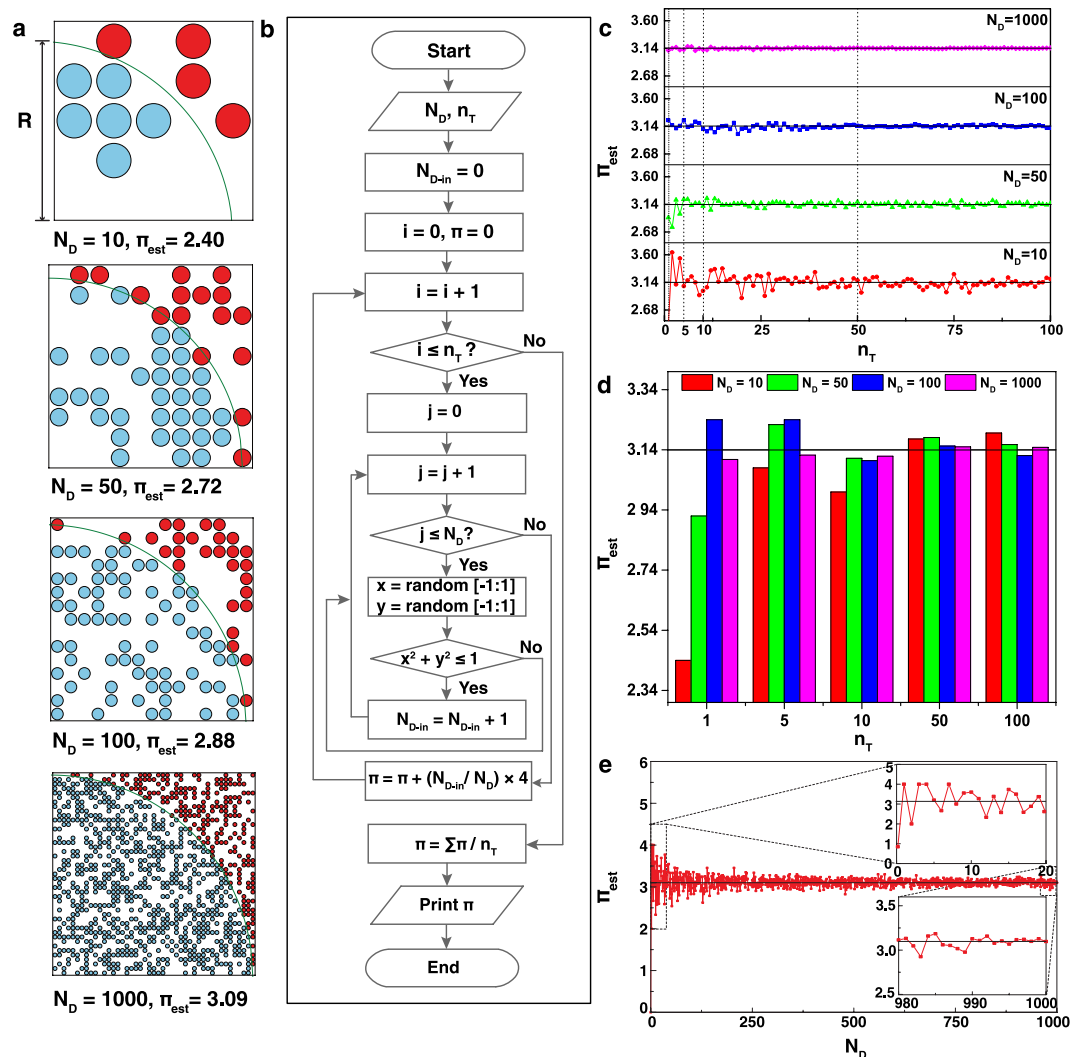


Figure 1. Calculation of π using Monte Carlo simulation. **(a)** The representative schematics for π calculation with a different number of dots in a square. Calculated numerical value of π ($=\pi_{est}$, where est stands for estimation) is defined as $(N_{D-in}/N_D) \times 4$, where N_{D-in} and N_D stand for the number of dots inside a quadrant of a circle (with a radius of R) and the total number of dots in a square (with a length of R). By definition, π_{est} with four different N_D , *i.e.* 10, 50, 100, and 1000 are calculated to be 2.40 ($=6/10 \times 4$), 2.72, 2.88 and 3.09 respectively, showing that roughly larger N_D gives a more accurate known value of π ($\pi_{known} \approx 3.14$). **(b)** A flow chart depicting algorithmic steps to obtain π_{est} with various N_D and total number of trials (n_T). **(c)** π_{est} as a function of n_T at a given N_D (*e.g.* 10, 50, 100, or 1000). In general, π_{est} approaches to π_{known} with the increasing n_T at relatively larger N_D values, as expected. **(d)** π_{est} as a function of N_D at a fixed n_T (*e.g.* 1, 5, 10, 50, or 100 marked as a dotted line in **(c)**). From observation, π_{est} approaches to π_{known} with the increasing N_D at relatively smaller n_T but π_{est} is roughly independent with N_D at relatively larger n_T . **(e)** A representative graph of π_{est} as a function of N_D . As N_D is increased, fluctuation of π_{est} from π_{known} tends to decrease. Insets show tendencies of fluctuation of π_{est} in the two different ranges of N_D .

Here, we develop ways to calculate π and evaluate the applicable number of self-avoiding walk paths with the aid of the computational simulation. In addition, we experimentally demonstrate the calculation of π and evaluate applicable self-avoiding walk paths with two different DNA nanostructures (double crossover DNA lattices and DNA rings) and self-avoiding random DNA lattices (constructed by a three-point star DNA motif having a blunt-end), respectively. Finally, we analyze the trend of numerical π variations controlled by DNA concentration, the total number of trials, and the characteristic growth behaviour of self-avoiding random DNA lattices evaluated through the total number of growth steps for the self-avoiding walk path.

Results

Calculation of π value. The representative schematics for π calculation with a different number of dots in a square having a quadrant of a circle are shown in Fig. 1a. For acquiring an calculated numerical value of π ($=\pi_{est}$, where est stands for estimation), a random event needs to be considered which can be defined as drawing uniformly distributed dots (like throwing darts randomly at a board) over a square bounding box within the region

whose area is to be determined. By considering a quadrant of a circle with a radius R bounded by a square with a length R , the ratio of the quadrant area to the square area is approximately equal to the ratio of the total number of dots falling inside the quadrant (N_{D-in} , marked as blue) to the total number of dots inside the square (N_D) due to the uniformly distributed dots within the square. Therefore, π_{est} can be defined as $(N_{D-in}/N_D) \times 4$. By definition, representative π_{est} with four different N_D (*i.e.* 10, 50, 100, and 1000) are calculated to be 2.40 ($=6/10 \times 4$), 2.72, 2.88 and 3.09 respectively. This shows that a roughly larger N_D gives a relatively more accurate known value of π ($\pi_{known} \approx 3.14$). Consequently, the magnitude (*i.e.* 0.060 = $|3.2-3.14|$, 0.020, 0.019, and 0.001) of the deviation of π_{est} from π_{known} ($\Delta\pi_{exp} = |\pi_{est} - \pi_{known}|$) will be smaller as N_D (10, 50, 100, and 1000) increases at a given optimum N_{D-in} (*i.e.* 8, 39, 79, and 785, which provides the most accurate π_{est} compared to π_{known} at a given N_D).

Figure 1b shows a flowchart representing algorithmic steps in order to obtain π_{est} as a function of either N_D , or the total number of trials (n_T). By assigning an initial input of N_D with the unit-step increment of j , dots are randomly sampled in a square. Then, N_{D-in} are counted until j reaches to N_D followed by evaluation of π_{est} calculated as $(N_{D-in}/N_D) \times 4$. Similarly, when the unit-step increment of i reaches an initial input of n_T , summed π_{est} is divided by n_T to get the average π_{est} .

By using the algorithm for π_{est} , numerical values of the π_{est} as functions of N_D and n_T can be obtained and analyzed. π_{est} as a function of n_T at four different N_D values (*i.e.* 10, 50, 100, and 1000) are obtained, which approaches π_{known} with the increasing n_T at any given N_D values, as expected (Fig. 1c). The π_{est} with varying N_D at a fixed n_T (*e.g.* 1, 5, 10, 50, or 100 marked as a dotted line in Fig. 1c) are extracted in order to evaluate the trend of π_{est} as a function of N_D which shows that π_{est} heavily relies on N_D at relatively smaller n_T but it is roughly independent of N_D at larger n_T (Fig. 1d). A representative graph of π_{est} as a function of N_D is shown in Fig. 1e. As N_D is increased, the fluctuation of π_{est} from π_{known} tends to decrease. Insets show the fluctuation tendency of π_{est} in the two different ranges of N_D (*i.e.* between 0~20 and 980~1000), which clearly shows that fluctuation of π_{est} from π_{known} tends to decrease with the increase in N_D , as expected. In addition, the differentiation of π_{est} per unit number of dots ($=\Delta\pi_{est}/\Delta N_D$) as a function of N_D is shown in Supplementary Fig. 1. Differences in the π_{est} per unit number of dots tend to decrease with the increase in N_D because π_{est} at a relatively larger N_D has a greater chance to give an accurate value of π .

Experimental observation of π using DNA nanostructures. Experimental observation of π (π_{exp}) is demonstrated by constructing two types of DNA nanostructures, *i.e.* double crossover (DX) DNA lattices^{33,34} and DNA rings³⁵⁻³⁷ (Fig. 2). Two sets of DX DNA motifs (*i.e.* PR and PS) are designed for construction of DX DNA lattices. Here, P stands for Pi (π) and R/S indicate opposite helical directionalities of the duplexes within the motifs (See Supplementary Fig. 2, Supplementary Tables 1 and 2). Each set has two DX motifs, without and with hairpins marked as PR(S)0 and PR(S)1, respectively (Fig. 2a). A DX motif having hairpins ~3.5 nm long protruding up and down is called DXH (*i.e.* PR1 and PS1). DX and DXH motifs, having identical sets of sticky ends in each set with the equal probability of binding (two exemplified binding sites are indicated by question marks in Fig. 2b), can hybridize to form a DX lattice with the aid of complementary colour-coded and shape-coded sticky ends. In addition, DNA rings comprised of T motifs (non-crossover based DNA motifs having three double-stranded domains connected through single strands. See Fig. 2c, Supplementary Fig. 3, and Supplementary Tables 3 and 4) are fabricated in order to obtain π_{exp} . A ring with inner and outer diameters of 13 nm and 29 nm is constituted through the complementary base-pairs of the sticky ends in T motifs (Fig. 2d).

Representative structural configurations of DX DNA lattices and DNA rings are shown in Fig. 2e,h, respectively. Atomic force microscope (AFM) images of DX lattices with different concentrations of DXH (0, 25, 50, 100, 150, and 200 nM symbolized as DXH₀, DXH_{0.25}, DXH_{0.5}, DXH_{1.0}, DXH_{1.5}, and DXH_{2.0}, respectively) were annealed in free solution. An arc (shown in blue) in each image is drawn representing the first quadrant in a circle. π_{exp} (0.00, 3.26, 3.27, 3.50, 2.98, 3.32, and 3.13) through images in Fig. 2e are obtained by $(N_{H-in}/N_H) \times 4$, where N_{H-in} and N_H represent the number of hairpins inside a quadrant of a circle and total number of hairpins in an image. Four circle quadrants can be assigned on a given image, which provide specific π_{exp} . DXH concentration ([DXH])-dependent N_H values (roughly linearly dependent) obtained by theoretical calculation and analyzed by AFM images are displayed in Fig. 2g. Similarly, AFM images of DNA rings with different concentrations of a T motif (1, 2, 5, 8, 10, and 20 nM indicated as R₁, R₂, R₅, R₈, R₁₀, and R₂₀, respectively) were annealed through a mica-assisted growth method³⁸⁻⁴⁰ (Fig. 2h). Arcs are drawn in third quadrants and corresponding π_{exp} (ranging between 2.75 and 3.20 measured by $(N_{R-in}/N_R) \times 4$, where N_{R-in} and N_R indicate number of rings inside a quadrant and total number of rings in an image) are shown in the images. Lastly, a plot of N_R as a function of [T] (roughly sigmoidal) analyzed by AFM images is shown in Fig. 2i.

Analysis of π using experimental observation. The analysis of π_{exp} controlled by [DX] and n_T are conducted and results are displayed in Fig. 3. The histogram in Fig. 3a shows an average of π_{exp} ($\langle\pi_{exp}\rangle$) obtained from more than four data sets at a given [DXH] as a function of [DXH] (the concentration sum of DXHs in each set of motif, $[DX_{PR1}] + [DX_{PS1}]$) *i.e.* 25, 50, 75, 100, 150, and 200 nM at a fixed $[DX_{PR}]$ and $[DX_{PS}]$ of 100 nM. For example, 150 nM of [DXH] indicates 150 nM of $[DX_{PR1}] + [DX_{PS1}]$ with 50 nM of $[DX_{PR0}] + [DX_{PS0}]$. Although the standard deviation of an error bar generally decreases as [DXH] increases, the magnitude of the deviation of π_{exp} from π_{known} ($\Delta\pi_{exp} \equiv |\pi_{exp} - \pi_{known}|$) is almost constant above 50 nM of [DXH]. A plot of π_{exp} as a function of [DX] ($= [DX_{PR(S)}]$) with $[DX_{PR(S)0}] = [DX_{PR(S)1}]$ is shown in Fig. 3b. By observation, 100 nM of [DX] gives a more accurate π_{exp} ($\Delta\pi_{exp}$ of ~0.009) than 50 (~0.062) or 200 nM (~0.049) of [DX]. Figure 3c displays $\Delta\pi_{exp}$ (arranged in a descending order) and $\langle\pi_{exp}\rangle$ (defined as $\sum_{n=1}^{n_T} \pi_{exp} / n$) as a function of n_T at a fixed [DX] of 100 nM which provide the general behaviour of π_{exp} approaching π_{known} with increasing n_T , as expected.

Similarly, π_{exp} and $\Delta\pi_{exp}$ as functions of [T] and n_T analysed from DNA rings are discussed. As observed from the bar graph of π_{exp} in Fig. 3d, the standard deviation of an error bar roughly decreases as [T] increases and $\Delta\pi_{exp}$ is approximately independent with [T], which might be due to the uniform distribution of the DNA rings on a

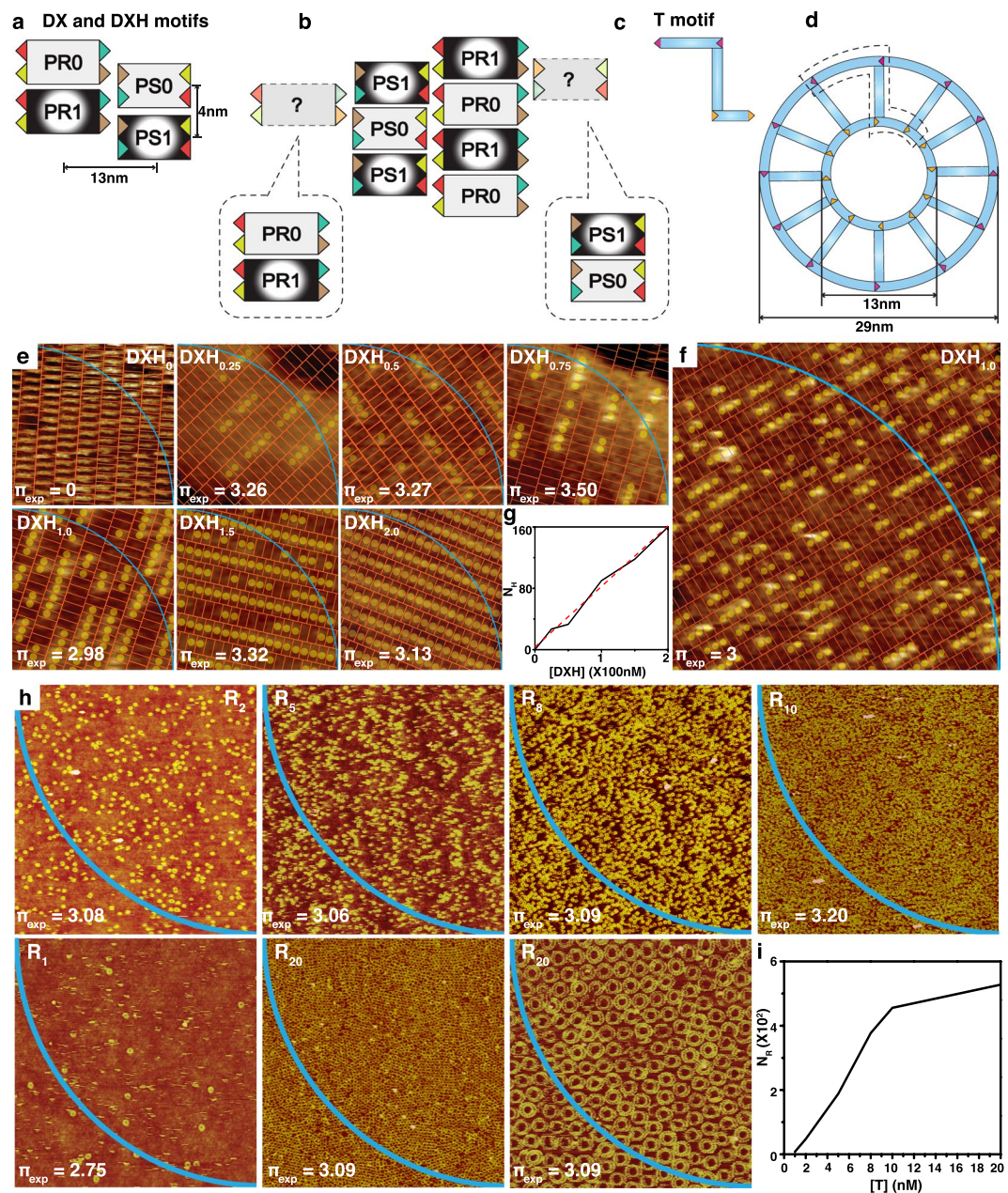


Figure 2. Experimental observation of π using DNA nanostructure configuration. **(a,b)** Cartoon representations of two sets – PR and PS – of DNA double-crossover (DX) motifs and corresponding DX lattice formed by complementary colour-coded sticky ends. Each set has two DX motifs, without and with hairpins marked as PR(S)0 and PR(S)1, respectively. Hairpins with a length of 3.5 nm protruding up and down on a DX motif called as a DXH. DX and DXH motifs having identical sets of sticky ends in each set can hybridize to form a DX lattice (two exemplified binding sites are indicated by question marks) with the equal probability of binding. **(c,d)** Schematics of unit building block (called as a T motif) and a DNA ring made of T motifs. The complementary-counterparts are colour-coded with the same colours. **(e,f)** AFM images of DX lattices with different concentrations of DXH (0, 25, 50, 100, 150 and 200 nM represented as DXH₀, DXH_{0.25}, DXH_{0.5}, DXH_{1.0}, DXH_{1.5} and DXH_{2.0} respectively) annealed in free solution. An arc (shown in blue) in each image is drawn representing first quadrant in a circle. Experimental observation of π through images (π_{exp}) can be obtained by $(N_{\text{H-in}}/N_{\text{H}}) \times 4$, where $N_{\text{H-in}}$ and N_{H} represent the number of hairpins inside a quadrant of a circle and total number of hairpins in an image. A scan size of all images in **(e,f)** is $100 \times 100 \text{ nm}^2$ ($200 \times 200 \text{ nm}^2$). **(g)** A graph of concentration of DXH ([DXH]) dependent N_{H} analyzed by AFM images with the scan size of $100 \times 100 \text{ nm}^2$. Theoretical and experimental N_{H} are plotted as red-dotted and black-solid lines, respectively. **(h)** AFM images of DNA rings with different concentrations of a T motif (2, 5, 8, 10 nM with the scan size of $3 \times 3 \mu\text{m}^2$, 1 and 20 nM with $2 \times 2 \mu\text{m}^2$, and 20 nM with $600 \times 600 \text{ nm}^2$ indicated as R₂, R₅, R₈, R₁₀, R₁, R₂₀ and R₂₀, respectively) annealed through a mica-assisted growth method. Arcs are drawn in third quadrants and corresponding π_{exp} (measured by $(N_{\text{R-in}}/N_{\text{R}}) \times 4$, where $N_{\text{R-in}}$ and N_{R} represent number of rings inside a quadrant and the total number of rings in an image) are shown in images. **(i)** A plot of N_{R} as a function of [T] analyzed by AFM images with scan size of $1 \times 1 \mu\text{m}^2$.

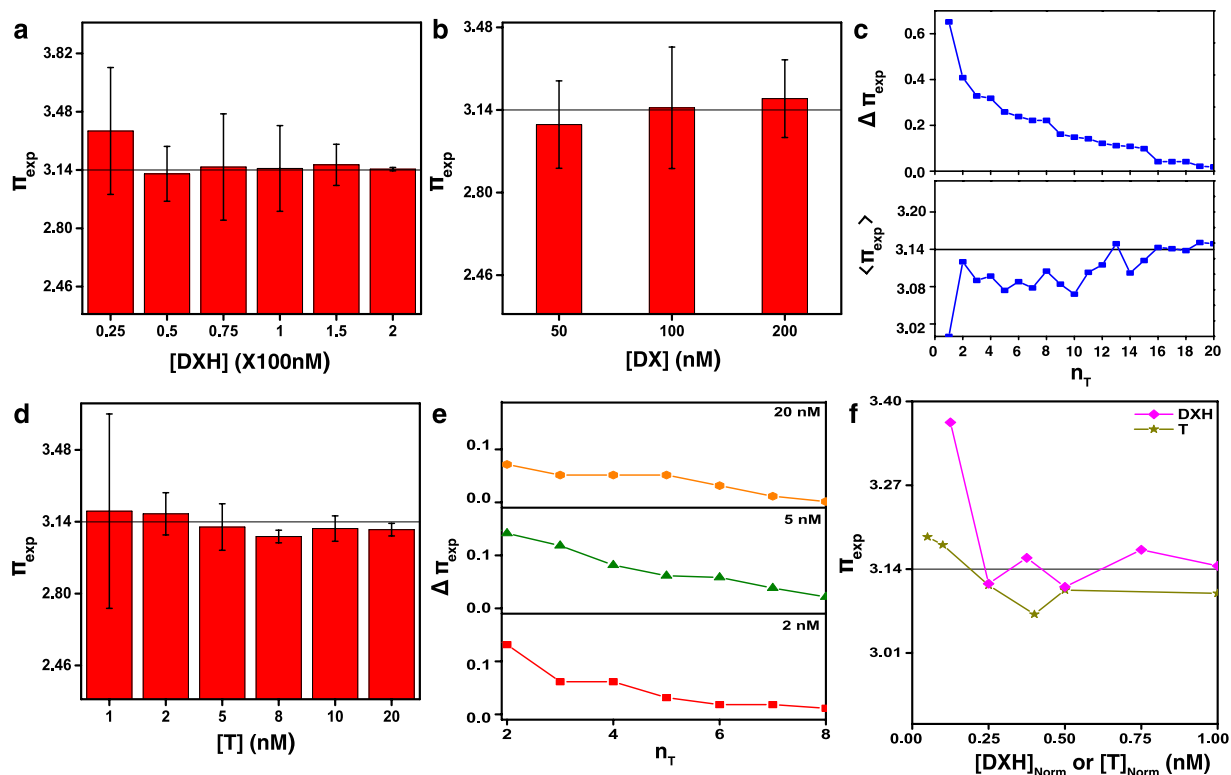


Figure 3. The analysis of experimentally obtained π (π_{exp}) controlled by DNA concentrations ([DNA]) and the number of trials (n_T). **(a)** A histogram plot of π_{exp} as a function of concentrations of a DX motif with the hairpin ([DXH]) at a fixed concentration of each motif set ($[\text{DX}_{\text{PR}}] = [\text{DX}_{\text{PS}}] = 100$ nM). Here, [DXH] is defined as the concentration sum of DXHs in each set of motif ($=[\text{DX}_{\text{PR}1}] + [\text{DX}_{\text{PS}1}]$). For instance, 50 nM of [DXH] means 50 nM of $[\text{DX}_{\text{PR}1}] + [\text{DX}_{\text{PS}1}]$ with 150 nM of $[\text{DX}_{\text{PR}0}] + [\text{DX}_{\text{PS}0}]$. Average π_{exp} is obtained from more than four data sets at a given [DXH]. The magnitude of the deviation of π_{exp} from π_{known} ($\Delta\pi_{\text{exp}} = |\pi_{\text{exp}} - \pi_{\text{known}}|$) is almost constant above 50 nM of [DXH]. **(b)** A plot of π_{exp} as a function of [DX] ($=[\text{DX}_{\text{PR}}]$ or $[\text{DX}_{\text{PS}}]$) with the condition of $[\text{DX}_{\text{PR}}] = [\text{DX}_{\text{PS}}]$ with the equal amount of DX motifs without and with hairpins ($[\text{DX}_{\text{PR}0}] = [\text{DX}_{\text{PR}1}]$ and $[\text{DX}_{\text{PS}0}] = [\text{DX}_{\text{PS}1}]$). As an example, 100 nM of [DX] indicates $[\text{DX}_{\text{PR}}] = [\text{DX}_{\text{PS}}] = 100$ nM having 50 nM of each $[\text{DX}_{\text{PS}0}]$ and $[\text{DX}_{\text{PS}1}]$ as well as 50 nM each of $[\text{DX}_{\text{PR}0}]$ and $[\text{DX}_{\text{PR}1}]$. By observation, 100 nM of [DX] gives more accurate π_{exp} (3.15) than 50 (3.08) or 200 nM (3.19) of [DX]. **(c)** Plots of the deviation of π_{exp} ($\Delta\pi_{\text{exp}}$) (arranged in a descending order) and average π_{exp} ($\langle\pi_{\text{exp}}\rangle = \sum_{n=1}^{n_T} \pi_{\text{exp},n} / n$) as a function of n_T . Here, 100 nM of [DX] ($=[\text{DX}_{\text{PR}}] = [\text{DX}_{\text{PS}}]$) with 50 nM of each $[\text{DX}_{\text{PR}(S)0}]$ and $[\text{DX}_{\text{PR}(S)1}]$ are used. **(d)** A histogram plot of π_{exp} as a function of [T]. Accidentally, $\Delta\pi_{\text{exp}}$ are roughly independent of [T]. **(e)** Plots of $\Delta\pi_{\text{exp}}$ arranged in a descending order as a function of n_T at 2, 5, and 20 nM of [T]. Although 20 nM of [T] shows slightly less $\Delta\pi_{\text{exp}}$ than other [T], roughly $\langle\pi_{\text{exp}}\rangle$ are independent with [T] which is in agreement with **(d,f)** A graph of π_{exp} against normalized [DXH] ($[\text{DXH}]_{\text{Norm}} = [\text{DXH}] / [\text{DXH}]_{200}$) and normalized [T] ($[\text{T}]_{\text{Norm}} = [\text{T}] / [\text{T}]_{20}$). It shows comparison of π_{exp} with the two different DNA nanostructure configurations (*i.e.* lattices and rings).

given substrate. Curves of $\Delta\pi_{\text{exp}}$ arranged in a descending order as a function of n_T at 2, 5, and 20 nM of [T] are displayed in Fig. 3e. Although 20 nM of [T] shows slightly less $\Delta\pi_{\text{exp}}$ than other [T], roughly $\langle\pi_{\text{exp}}\rangle$ are independent from [T] which is in good agreement with Fig. 3d. π_{exp} against normalized [DXH] ($[\text{DXH}]_{\text{Norm}} = [\text{DXH}] / [\text{DXH}]_{200}$) and normalized [T] ($[\text{T}]_{\text{Norm}} = [\text{T}] / [\text{T}]_{20}$) are shown in Fig. 3f in order to compare π_{exp} with respect to either largest [DXH] or [T], as well as to understand comparison of π_{exp} with the two different DNA nanostructure configurations, *i.e.* DNA lattices and DNA rings.

Self-avoiding random lattice growth. A self-avoiding random walk path (called a lattice configuration) constructed by a unit building block is demonstrated via MC simulation in order to understand the feasibility to predict proper paths. A self-avoiding random lattice has a growth path on a lattice configuration that does not visit the same place more than once. Schematics of various lattice configurations constructed by a three-point star motif having single blunt-end (3PS_b) are represented in Fig. 4a. A blunt-end in a 3PS_b , which is introduced to generate asymmetric self-avoiding random lattices, is marked with a black (serves as a seed), a red (grown to the left), or a green dot (grown to the right). Formation of a self-avoiding random lattice starts from a seed 3PS_b ($N_s = 0$, where N_s indicates a step number) through the arrow facing of the incoming 3PS_b from the next step. Lattice configurations are named as (a step number, N_s)-(configuration number from the previous step)-(configuration number at the present step). For examples, 2-3-1 and 3-34-2 indicate 1st configuration of 2nd step obtained from 3rd configuration in 1st step for 2-3-1, and 2nd configuration of 3rd step obtained from 3rd configuration in

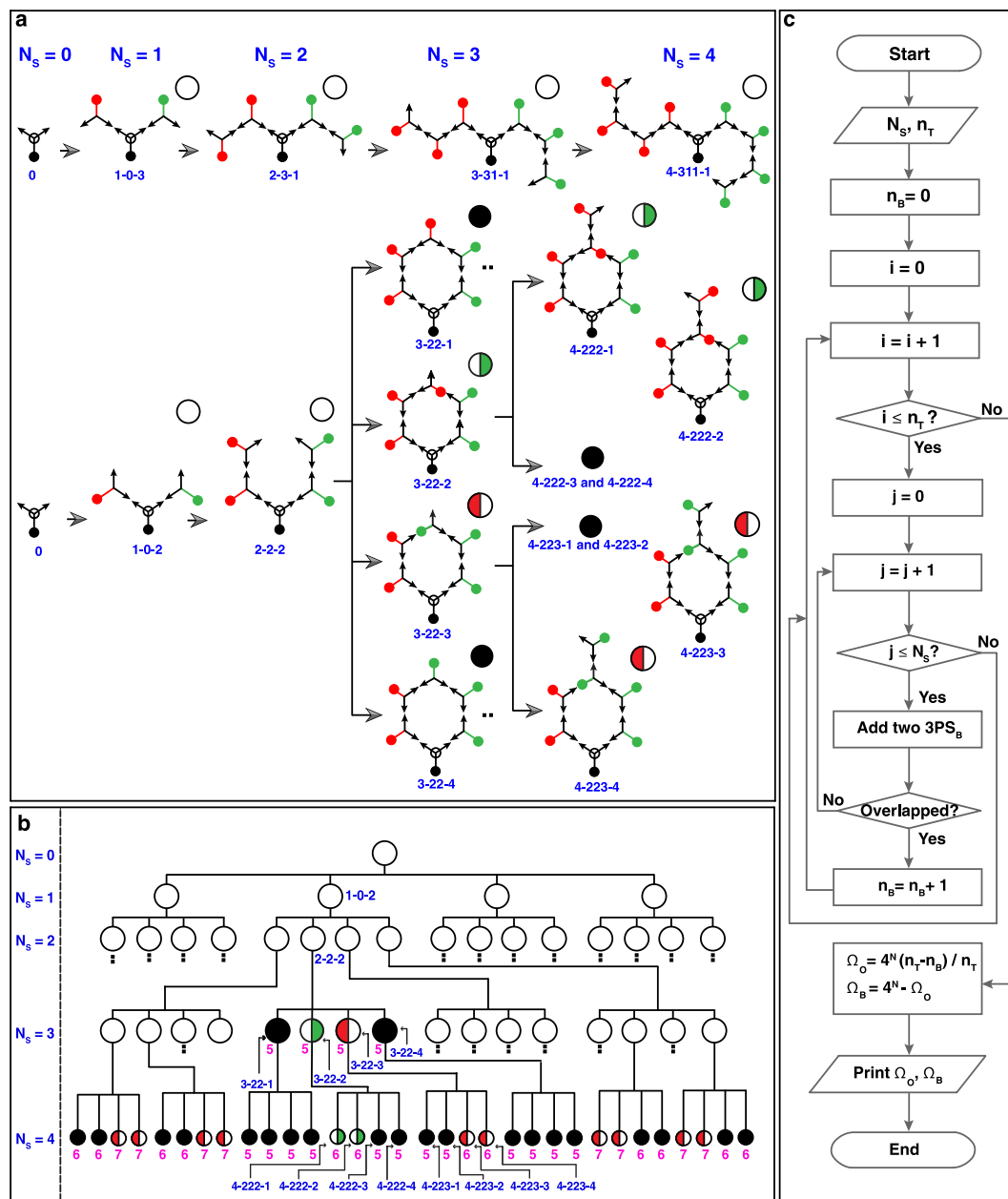


Figure 4. Lattice configuration of self-avoiding random lattice growth demonstrated with the three-point star motif having a blunt-end. **(a)** Schematic representations of lattices constructed by a three-point star motif having a blunt-end (3PS_B). A blunt-end is marked with either a black (served as a seed), a red (grown to the left), or a green dot (grown to the right). Lattice configurations are named as (step number, N_s)-(configuration number from the previous step)-(configuration number at the present step). For instance, 2-3-1 represents 1st configuration of 2nd step obtained from 3rd configuration in 1st step. There are two types of available lattice configurations, *i.e.* open and blocked (half- and full-blocked indicated by half- and fully-filled circles, respectively) lattice configurations. **(b)** A pedigree lattice configuration chart of self-avoiding random growth. 32 blocked lattice configurations – 10 (2) half-blocked happened on the left (right) side of the lattices, and 20 full-blocked configurations – out of 256 available configurations ($\Omega_{N_s} = 4^{N_s}$) after 4th step (N_s = 4) of lattice growth are shown. Total number of the 3PS_B (excluding a seed 3PS_B) participated in that configuration is indicated by magenta. **(c)** A flow chart depicting algorithmic steps to obtain the total numbers of open (Ω_o) and blocked (Ω_b) lattice configurations at a given N_s.

1st step and 4th configuration in 2nd step for 3-34-2. All possible lattice configurations up to N_s = 3 are shown in Supplementary Fig. 4. In order to predict applicable numbers of self-avoiding lattices, available lattice configurations at a given N_s are analyzed. There are two types of available lattice configurations, *i.e.* an open, marked as a hollow circle and a blocked lattice configuration marked as either a half-filled (with red for left-blocked or green for right-blocked configurations) or a fully-filled circle as shown in Fig. 4a. Open, half-blocked, and full-blocked

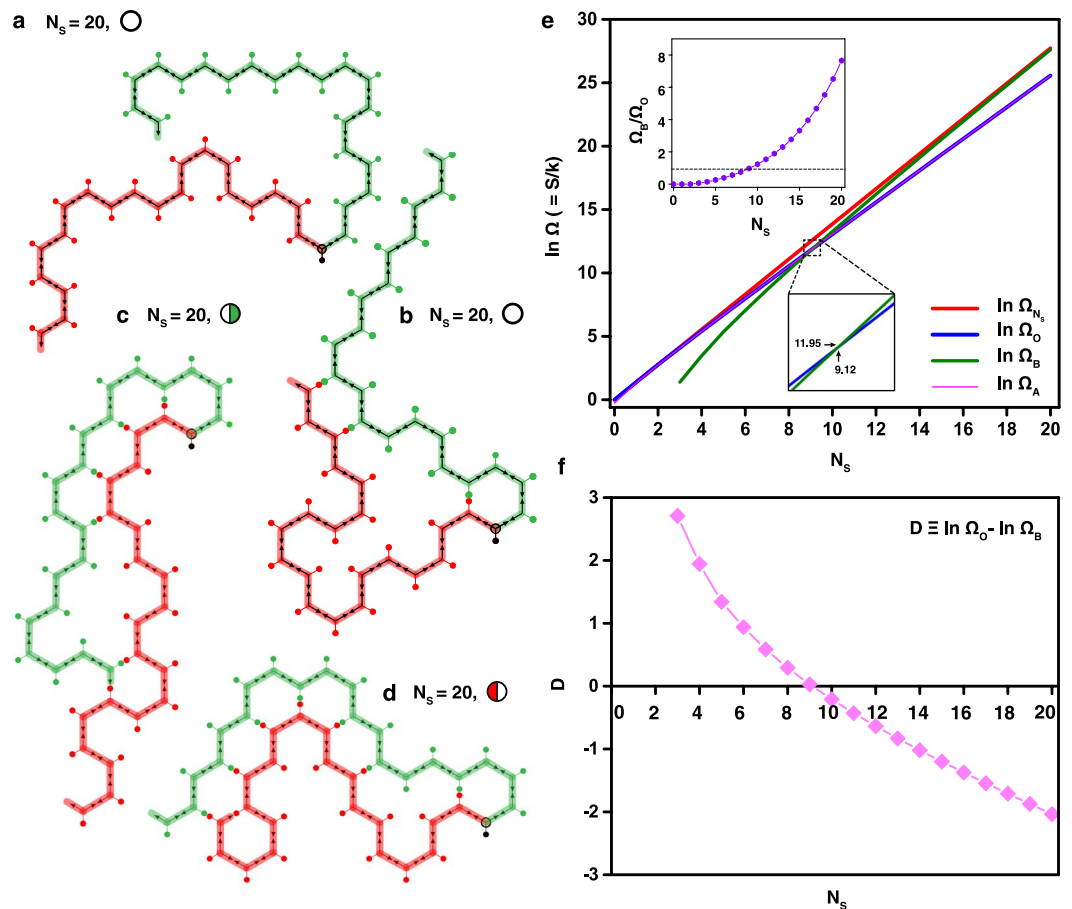


Figure 5. Representative lattice configurations and analysis of self-avoiding random lattice growth generated by the self-avoiding walk algorithm. (a–d) Lattice configurations of self-avoiding random growth at a N_s of 20. Open (a,b) and half-blocked configurations (growth blocked on either the right (c) or left (d) side of the lattices) are displayed. (e) Logarithmic numbers of lattice configurations ($\ln \Omega = S/k$, where S is entropy and k is a constant) as a function of N_s . $\ln \Omega$ obtained from the total numbers of available, open, and blocked (including half- and full-blocked) lattice configurations ($\Omega_{N_s} = 4^{N_s}$, Ω_O , and Ω_B , respectively) at a given N_s as well as from analytical evaluation of open lattice configuration (Ω_A) are depicted. The intersection between $\ln \Omega_O$ and $\ln \Omega_B$ (occurred at 9.12 of N_s) and the ratio of Ω_B and Ω_O are shown in the bottom and top insets, respectively. Ω_O is larger and smaller than Ω_B at below and above regions of the thin dotted line (marked at $\Omega_B/\Omega_O = 1$ in the graph of Ω_B/Ω_O), respectively. (f) A graph of difference of $\ln \Omega_O$ and $\ln \Omega_B$ ($D \equiv \ln \Omega_O - \ln \Omega_B$) as a function of N_s . As mentioned, D becomes 0 at N_s of 9.12 and the magnitude of D increases noticeably as N_s increases or decreases from 9.12.

lattice configurations are easily determined by counting available numbers of arrows (binding sites for the next step) in a lattice (*i.e.* 2, 1, and 0 arrows in the lattices indicate open, half-, and full-blocked lattice configurations, respectively).

Overall self-avoiding random lattice configurations are represented by a pedigree chart in Fig. 4b. Although all blocked lattice configurations (up to $N_s = 4$) are fully displayed, some open configurations are skipped (indicated by dots) for clarity. Total numbers of open (Ω_O) and blocked (full- and half-blocked) (Ω_B) lattice configurations at $N_s = 3$ are 60 and 4 (2 and 2) among 64 available configurations ($\Omega_{N_s} = 4^3$). Similarly, there are 224 open and 32 blocked lattice configurations (20 full-blocked and 12 half-blocked configurations (10 happened on the left side of the lattice and 2 on the right)) out of 256 ($\Omega_{N_s} = 4^3$) at the 4th step of lattice growth. The total number of 3PS_B (excluding a seed 3PS_B) that participated in specific lattice configurations varied with (and even within) N_s , which are indicated by magenta in the pedigree chart. Figure 4c shows a flowchart with algorithmic steps for acquiring Ω_O and Ω_B as a function of N_s . By initially assigning the total number of trials (n_T) and N_s with i and j for the unit-step increments of the trial and the step respectively, $\Omega_O (= 4^{N_s} \times (n_T - n_B)/n_T$, where n_B is the number of trials giving blocked lattice configurations) and $\Omega_B (= 4^{N_s} - \Omega_O)$ at a given N_s are counted until i reaches to n_T .

Analysis of self-avoiding random lattice configurations. Physical configurations of self-avoiding random lattices with the symbolic representations of configurations grown up to N_s of 20 (50 and 100) generated by the self-avoiding walk algorithm are shown in Fig. 5a–d (Supplementary Figs 5 and 6). Two-dimensional

self-avoiding random lattices are self-assembled through the subsequent $3PS_B$ bindings to a seed tile of $3PS_B$, which has two binding sites, left and right leading the paths of the red and green, respectively. Here, open, half-blocked (growth blocked on either the left (a red path) or right (a green) side of the lattice), and full-blocked configurations are symbolized by a hollow, half-filled and fully-filled circle, respectively.

Figure 5e and f show logarithmic numbers of lattice configurations ($\ln \Omega = S/k$, where S is entropy and k is a constant) and its difference for open and blocked self-avoiding random lattice configurations as a function of N_s . $\ln \Omega_{N_s}$, $\ln \Omega_O$, and $\ln \Omega_B$ are easily obtained from the total number of available, open, and blocked (including half-blocked and full-blocked) lattice configurations (*i.e.* $\Omega_{N_s} = 4^{N_s}$, Ω_O , and Ω_B) respectively at a given N_s . In addition, the total number of open lattice configurations (Ω_A) for a 2-dimensional hexagonal lattice model can be analytically extracted ($\Omega_A = 0.415 \cdot (\sqrt{2} + \sqrt{2})^{2N_s+1} \cdot (2N_s + 1)^{\frac{11}{32}}$), as shown in Fig. 5e²⁴. Although $\ln \Omega_O$ and $\ln \Omega_A$ differ by ~3% at relatively smaller N_s , they tend to overlap completely with the difference percentage ratio ($100 \times |\ln \Omega_A - \ln \Omega_O| / \ln \Omega_A$) of $\sim 10^{-2}\%$ at larger N_s . The intersection between $\ln \Omega_O$ and $\ln \Omega_B$ (occurred at 9.12 of N_s) and the ratio of Ω_B and Ω_O are shown in the bottom and top insets, respectively. Ω_O is larger and smaller than Ω_B at below and above regions of the thin dotted line (marked at $\Omega_B/\Omega_O = 1$ in the graph of Ω_B/Ω_O), respectively. In order to compare occurrences of open and blocked lattice configurations, difference (D) of $\ln \Omega_O$ and $\ln \Omega_B$ as a function of N_s are discussed (Fig. 5f). As mentioned, D becomes 0 at N_s of 9.12 and magnitude of D increases with increasing or decreasing N_s from the cross point at $N_s = 9.12$.

Experimental observation of self-avoiding random lattices. Three different DNA nanostructures (a honeycomb lattice, a hexagonal ring, and a three-point star dimer) are constructed by slightly modified three-point star DNA motifs in order to test their applicability in the growth of self-avoiding random lattices (See Fig. 6, Supplementary Fig. 7, and Supplementary Table 5). Figure 6a shows a schematic of a three-point star DNA motif ($3PS_{HL}$) for construction of a honeycomb lattice (a simplified one shown at a right bottom) and its representative AFM image of a honeycomb lattice. A $3PS_{HL}$ is comprised of 7 strands (marked as #1~#7) with palindromic self-complementary sticky-end sequences (indicated as S1, S2, and S3) located at the end of each arm^{41,42}. Schematics and representative AFM images of three-point star DNA motifs with a single ($3PS_{HR}$, for fabrication of a hexagonal ring) and double blunt ends ($3PS_D$, for formation of a 3PS dimer) are shown in Fig. 6b and c. A $3PS_{HR}$ (a black dot in simplified $3PS_{HR}$ indicates a blunt end arm as shown in Fig. 6b) and a $3PS_D$ (two black dots in simplified $3PS_D$ represent the blunt end arms in Fig. 6c) need 6 strands (strand #7 removed from $3PS_{HL}$) with two sets (S1 and S2) of palindromic self-complementary sticky-end sequences, and 5 strands (#6 and #7 removed from $3PS_{HL}$) with a single set (S1) of palindromic self-complementary sticky-end sequences, respectively. From the observation of the AFM images, honeycomb lattices, hexagonal rings, and 3PS dimers are well formed in agreement with the design schemes with relatively higher production yields than cross-tile lattices made of four-point star motifs⁴³.

Figure 6d–s show the representative experimental results and analysis of self-avoiding random lattices grown by the 3PS DNA motifs ($3PS_B$). In $3PS_B$, a #6 strand from $3PS_{HL}$ is removed and self-complementary sticky-end sequences in #7 are replaced from S3 to S1. A blunt-end in a simplified $3PS_B$ shown in the right bottom of Fig. 6d is marked with either a black (served as a seed), a red (grown to the left), or a green dot (grown to the right) in order to easily evaluate the lattice configurations. Representative AFM images with the lattice configurations (either an open, a half-blocked or a full-blocked configuration at a given step number) of self-avoiding random lattices comprised of $3PS_B$ are displayed in Fig. 6e–p. Simplified $3PS_B$ motifs are overlaid on AFM images to enhance the visibility of lattice configurations. Figure 6r,s display percentages of the total number of $3PS_B$ motifs (α) in specific ranges (*i.e.* below 10, 11–20, 21–30, and above 30) and percentages of total number of open, half-blocked and full-blocked lattice configurations (β) obtained from the AFM data. Although it would be difficult to form relatively larger self-avoiding lattices due to the existence of a blunt end in a $3PS_B$, as we anticipated, interestingly we observe that lattices having more than 31 numbers of $3PS_B$ are dominant (38.5% among all evaluated lattices). In addition, the percentages of lattice configurations in the range of 3 to 49 of N_s are examined. Open (blocked) lattice configurations are dominant below (above) $N_s = 9.12$, which agree well with the simulation results discussed in Fig. 5e,f.

Discussion

We discuss methodologies to calculate the numerical value of π and to evaluate a possible number of self-avoiding walk paths with the aid of computational MC simulation. Additionally, we demonstrate the calculation of π and evaluation of applicable self-avoiding walk paths by distinct DNA nanostructures. Finally, we analyze the trend of numerical variations of π as functions of DNA concentration and the total number of trials for π calculation, and the behaviour of self-avoiding random DNA lattice growth evaluated through number of growth steps for the self-avoiding walk path. From observation of experimental calculations of π (π_{exp}) demonstrated by constructing two different types of DNA nanostructures (*i.e.* double crossover DNA lattices and DNA rings), fluctuation of π_{exp} from known π tends to decrease as either DNA concentration or the number of trials increases. Based upon experimental observation of self-avoiding random lattices grown by the three-point star DNA motifs, the percentage of lattice configurations is examined. Open (blocked) lattice configurations are dominant below (above) the step number of 9.12 (at this step number obtained by simulation, numbers of open and blocked configurations are the same). This in depth study of numerical calculation of mathematical constants and characteristic estimation of abstract models via DNA provides a novel perspective for the applicability of DNA in the field of science and engineering.

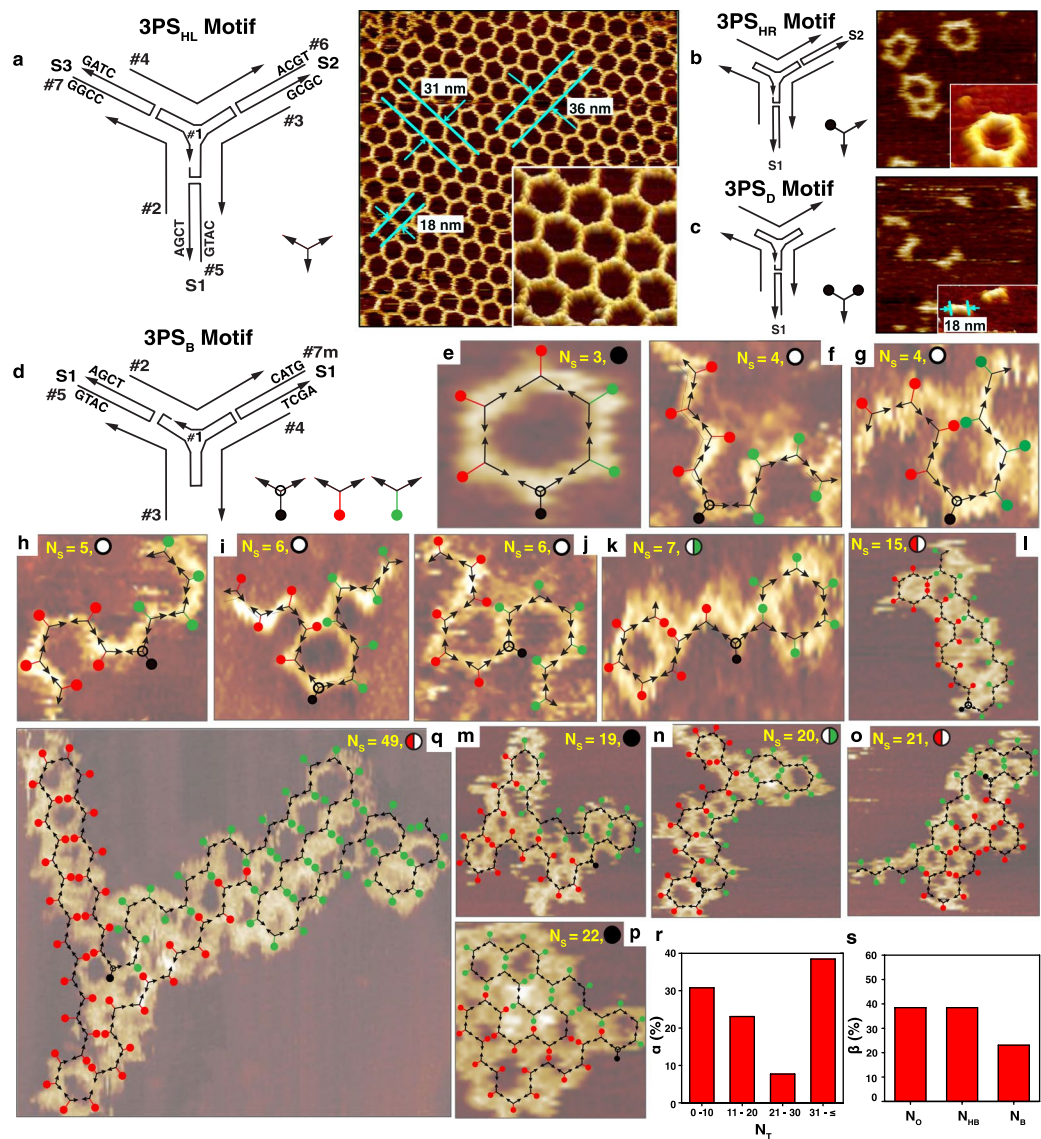


Figure 6. Experimental observation of self-avoiding random lattice growth with the three-point star DNA motif. (a) A schematic of a three-point star DNA motif ($3PS_{HL}$) for construction of a honeycomb lattice and its representative AFM image (scan size of $500 \times 500 \text{ nm}^2$) of a honeycomb lattice. Seven strands constituting $3PS_{HL}$ are numbered as #1~#7, where palindromic self-complementary sticky-end sequences located at the end of each arm are indicated as S1, S2, and S3. A simplified $3PS_{HL}$ and a magnified honeycomb lattice ($100 \times 100 \text{ nm}^2$) are shown at the right bottom corners of them. (b) A schematic of a three-point star DNA motif with a single blunt end ($3PS_{HR}$) for fabrication of a hexagonal ring and its AFM image. Six strands (strand #7 removed from $3PS_{HL}$) and two sets (S1 and S2) of palindromic self-complementary sticky-end sequences are required. A black dot in simplified $3PS_{HR}$ indicates a blunt end arm. Inset in AFM image is 3-dimensional visualization of a hexagonal ring. (c) A schematic of a three-point star DNA motif with double blunt ends ($3PS_D$) for formation of a 3PS dimer and its AFM image. Five strands (#6 and #7 removed from $3PS_{HL}$) and single set (S1) of palindromic self-complementary sticky-end sequences is required. Inset in AFM image is 3-dimensional visualization of 3PS dimers. (d) A schematic of a three-point star DNA motif with a blunt end ($3PS_B$) for demonstration of a self-avoiding random lattice. Strand #6 is removed from $3PS_{HL}$ and self-complementary sticky-end sequences in #7 are modified. A blunt-end in a simplified $3PS_B$ is marked with a black (served as a seed), a red (grown to the left), or a green dot (grown to the right) in order to easily analyze the lattice configurations. (e–q) Representative AFM images of self-avoiding random lattices comprised of $3PS_B$. Either an open, a half-blocked or a full-blocked lattice configuration at a given step number is indicated in each image. In order to clarify the growth visualization of lattice configurations, simplified $3PS_B$ are overlaid on AFM images. (r) A plot of percentage of total number of $3PS_B$ motifs (α) in that specific range, *i.e.* below 10, 11–20, 21–30, and above 30. (s) A bar graph of percentages of the total number of open, half-blocked, and a full-blocked lattice configurations (β).

Methods

DNA nanostructure fabrication. Synthetic oligonucleotides purified *via* high-performance liquid chromatography were purchased from Bioneer (Daejeon, Korea). Double-crossover (DX) DNA lattices were formed by the 2-step free solution annealing method. First, individual strands of either DX (without hairpins, PR0 and PS0) or DXH (with hairpins, PR1 and PS1) motif were mixed with equimolar concentration (800 nM) in $1 \times$ TAE/Mg²⁺ buffer solution (40 mM Tris, 20 mM Acetic acid, 1 mM EDTA (pH 8.0), and 12.5 mM magnesium acetate). These strand mixtures of each motif (*i.e.* PR0, PS0, PR1, and PS1) in the test tubes were then slowly cooled from 95 to 25 °C by placing them in a Styrofoam box containing 2 L of boiled water for about 2 days to facilitate hybridization. In succession, an appropriate amount of each motif was added into a new test tube to obtain DXH₀ DNA lattices (final concentrations of individual motifs were [PR0] = [PS0] = 100 nM, and [PR1] = [PS1] = 0 nM). Similarly, sets of motif concentrations ([PR0], [PS0], [PR1], and [PS1] = 75, 100, 25, and 0 nM; 50, 100, 50, and 0 nM; 25, 100, 75, and 0 nM; 50, 50, 50, and 50 nM; 0, 50, 100, and 50 nM; 0, 0, 100, and 100 nM) were prepared to construct DXH_{0.25}, DXH_{0.5}, DXH_{0.75}, DXH_{1.0}, DXH_{1.5}, and DXH_{2.0} DNA lattices, respectively. Second step annealing was performed by placing sample test tubes in a Styrofoam box containing 2 L of water (initial temperature, 40 °C) and cooling them from 40 °C to 25 °C for about 24 hours to obtain DX DNA lattices. (Fig. 2, Supplementary Fig. 2, Supplementary Tables 1 and 2)

DNA rings were formed by mixing a stoichiometric quantity of each strand in a buffer containing a mica substrate (size of 5×5 mm²). This strand mixture with mica was annealed in a test tube by slowly cooling from 95 to 25 °C in a Styrofoam box. Eventually, DNA rings formed on the mica surface with different coverages depending upon the concentration of a T motif. DNA rings with a five different T motif concentrations of 2, 5, 8, 10 and 20 nM were prepared and analyzed. (Fig. 2, Supplementary Fig. 3, Supplementary Tables 3 and 4)

Honeycomb lattices, hexagonal rings, 3PS dimers, as well as self-avoiding random lattices were constructed by specific three-point star motifs; 3PS_{HL}, 3PS_{HR}, 3PS_D, and 3PS_B motifs. They were formed by mixing stoichiometric quantities of each strand in the buffer by cooling from 95 °C to 25 °C in a Styrofoam box. Final concentrations of 3PS for all DNA nanostructure configurations were 200 nM. (Fig. 6, Supplementary Fig. 7, Supplementary Table 5)

AFM imaging. 5 μL of DNA nanostructures (*i.e.* DX lattices, honeycomb lattices, hexagonal rings, 3PS dimers, and self-avoiding random lattices) in buffer solution prepared *via* the free-solution annealing method were dropped on a freshly cleaved mica surface. A 30 μL of $1 \times$ TAE/Mg²⁺ buffer solution was then placed onto the mica, and another 20 μL was placed onto the silicon nitride AFM tip (NP-S10, Veeco Inc., CA, USA). To image DNA rings fabricated through the MAG method, a mica substrate with preformed DNA rings was taken from a test tube and placed on a metal puck. Then, 30 μL of buffer was pipetted onto the mica substrate, and another 20 μL was dispensed onto an AFM tip. Corresponding AFM images were then obtained using a Multimode Nanoscope (Veeco Inc., CA, USA) in the fluid-tapping mode (Figs 2 and 6).

References

- Niederreiter, H. *Random Number Generation and quasi-Monte Carlo Methods*. (Society for Industrial and Applied Mathematics, 1992).
- Fujibayashi, K. & Murata, S. Precise Simulation Model for DNA Tile Self-Assembly. *IEEE Trans. Nanotechnol.* **8**, 361–368 (2009).
- Bombelli, F. B. *et al.* DNA Closed Nanostructures: A Structural and Monte Carlo Simulation Study. *J. Phys. Chem. B* **112**, 15283–15294 (2008).
- Ouldrige, T. E., Johnston, I. G., Louis, A. A. & Doye, J. P. K. The self-assembly of DNA Holliday junctions studied with a minimal model. *J. Chem. Phys.* **130**, 65101 (2009).
- Reinhardt, A. & Frenkel, D. Numerical evidence for nucleated self-assembly of DNA brick structures. *Phys. Rev. Lett.* **112**, 238103 (2014).
- Carlson, E., Orlandini, E. & Stella, A. L. Roles of Stiffness and Excluded Volume in DNA Denaturation. *Phys. Rev. Lett.* **88**, 198101 (2002).
- Arsuaga, J., Vázquez, M., Trigueros, S., Sumners, D. W. & Roca, J. Knotting probability of DNA molecules confined in restricted volumes: DNA knotting in phage capsids. *Proc. Natl. Acad. Sci.* **99**, 5373–5377 (2002).
- Fujimoto, B. S. & Schurr, J. M. Monte Carlo Simulations of Supercoiled DNAs Confined to a Plane. *Biophys. J.* **82**, 944–962 (2002).
- Jayaram, B. & Beveridge, D. L. Modeling DNA in Aqueous Solutions: Theoretical and Computer Simulation Studies on the Ion Atmosphere of DNA. *Annu. Rev. Biophys. Biomol. Struct.* **25**, 367–394 (1996).
- Sales-Pardo, M., Guimerà, R., Moreira, A. A., Widom, J. & Amaral, L. A. N. Mesoscopic modeling for nucleic acid chain dynamics. *Phys. Rev. E* **71**, 51902 (2005).
- Kim, J. S. *et al.* An evolutionary Monte Carlo algorithm for predicting DNA hybridization. *Biosystems* **91**, 69–75 (2008).
- Bois, J. S. *et al.* Topological constraints in nucleic acid hybridization kinetics. *Nucleic Acids Res.* **33**, 4090–4095 (2005).
- Richter, J., Adler, M. & Niemeyer, C. M. Monte Carlo simulation of the assembly of bis-biotinylated DNA and streptavidin. *Chem Phys Chem* **4**, 79–83 (2003).
- Dai, W., Hsu, C. W., Sciortino, F. & Starr, F. W. Valency dependence of polymorphism and polyamorphism in DNA-functionalized nanoparticles. *Langmuir* **26**, 3601–3608 (2010).
- Hsu, C. W., Largo, J., Sciortino, F. & Starr, F. W. Hierarchies of networked phases induced by multiple liquid-liquid critical points. *Proc. Natl. Acad. Sci. USA* **105**, 13711–13715 (2008).
- Dai, W., Kumar, S. K. & Starr, F. W. Universal two-step crystallization of DNA-functionalized nanoparticles. *Soft Matter* **6**, 6130–6135 (2010).
- Kim, A. J., Scarlett, R., Biancanello, P. L., Sinno, T. & Crocker, J. C. Probing interfacial equilibration in microsphere crystals formed by DNA-directed assembly. *Nat. Mater.* **8**, 52–55 (2009).
- Scarlett, R. T., Crocker, J. C. & Sinno, T. Computational analysis of binary segregation during colloidal crystallization with DNA-mediated interactions. *J. Chem. Phys.* **132**, 234705 (2010).
- Scarlett, R. T., Ung, M. T., Crocker, J. C. & Sinno, T. A mechanistic view of binary colloidal superlattice formation using DNA-directed interactions. *Soft Matter* **7**, 1912–1925 (2011).
- Bozorgui, B. & Frenkel, D. Liquid-Vapor Transition Driven by Bond Disorder. *Phys. Rev. Lett.* **101**, 45701 (2008).
- Martinez-Veracoechea, F. J., Bozorgui, B. & Frenkel, D. Anomalous phase behavior of liquid-vapor phase transition in binary mixtures of DNA-coated particles. *Soft Matter* **6**, 6136–6145 (2010).

22. Martinez-Veracoechea, F. J., Mladek, B. M., Tkachenko, A. V. & Frenkel, D. Design Rule for Colloidal Crystals of DNA-Functionalized Particles. *Phys. Rev. Lett.* **107**, 45902 (2011).
23. Leunissen, M. E. & Frenkel, D. Numerical study of DNA-functionalized microparticles and nanoparticles: Explicit pair potentials and their implications for phase behavior. *J. Chem. Phys.* **134**, 84702 (2011).
24. Chan, Y. & Rechnitzer, A. A Monte Carlo study of non-trapped self-avoiding walks. *J. Phys. Math. Theor.* **45**, 405004–16 (2012).
25. Buffon, G. L. L. *Histoire naturelle, générale et particulière servant de suite à l'histoire des animaux quadrupèdes* /. (De l'Imprimerie royale, 1777).
26. Lee, K. W. *et al.* A two-dimensional DNA lattice implanted polymer solar cell. *Nanotechnology* **22**, 375202 (2011).
27. Nam, J.-M., Thaxton, C. S. & Mirkin, C. A. Nanoparticle-based bio-bar codes for the ultrasensitive detection of proteins. *Science* **301**, 1884–1886 (2003).
28. Jung, J. *et al.* Approaches to label-free flexible DNA biosensors using low-temperature solution-processed InZnO thin-film transistors. *Biosens. Bioelectron.* **55**, 99–105 (2014).
29. Lu, Y., Goldsmith, B. R., Kybert, N. J. & Johnson, A. T. C. DNA-decorated graphene chemical sensors. *Appl. Phys. Lett.* **97**, 83107 (2010).
30. Rikken, G. L. J. A. A New Twist on Spintronics. *Science* **331**, 864–865 (2011).
31. Braun, E., Eichen, Y., Sivan, U. & Ben-Yoseph, G. DNA-templated assembly and electrode attachment of a conducting silver wire. *Nature* **391**, 775–778 (1998).
32. Rakitin, A. *et al.* Metallic Conduction through Engineered DNA: DNA Nanoelectronic Building Blocks. *Phys. Rev. Lett.* **86**, 3670–3673 (2001).
33. Rothmund, P. W. K., Papadakis, N. & Winfree, E. Algorithmic self-assembly of DNA Sierpinski triangles. *PLoS Biol.* **2**, e424 (2004).
34. Winfree, E., Liu, F., Wenzler, L. A. & Seeman, N. C. Design and self-assembly of two-dimensional DNA crystals. *Nature* **394**, 539–544 (1998).
35. Hamada, S. & Murata, S. Substrate-assisted assembly of interconnected single-duplex DNA nanostructures. *Angew. Chem. Int. Ed Engl.* **48**, 6820–6823 (2009).
36. Lee, J. *et al.* Size-controllable DNA rings with copper-ion modification. *Small Weinh. Bergstr. Ger.* **8**, 374–377 (2012).
37. Kim, J., Lee, J., Hamada, S., Murata, S. & Ha Park, S. Self-replication of DNA rings. *Nat. Nanotechnol.* **10**, 528–533 (2015).
38. Sun, X., Hyeon, K. S., Zhang, C., Ribbe, A. E. & Mao, C. Surface-Mediated DNA Self-Assembly. *J. Am. Chem. Soc.* **131**, 13248–13249 (2009).
39. Lee, J. *et al.* Coverage control of DNA crystals grown by silica assistance. *Angew. Chem. Int. Ed Engl.* **50**, 9145–9149 (2011).
40. Kim, B., Amin, R., Lee, J., Yun, K. & Park, S. H. Growth and restoration of a T-tile-based 1D DNA nanotrack. *Chem. Commun. Camb. Engl.* **47**, 11053–11055 (2011).
41. He, Y., Chen, Y., Liu, H., Ribbe, A. E. & Mao, C. Self-Assembly of Hexagonal DNA Two-Dimensional (2D) Arrays. *J. Am. Chem. Soc.* **127**, 12202–12203 (2005).
42. Yang, X., Wenzler, L. A., Qi, J., Li, X. & Seeman, N. C. Ligation of DNA Triangles Containing Double Crossover Molecules. *J. Am. Chem. Soc.* **120**, 9779–9786 (1998).
43. Yan, H., Park, S. H., Finkelstein, G., Reif, J. H. & LaBean, T. H. DNA-Templated Self-Assembly of Protein Arrays and Highly Conductive Nanowires. *Science* **301**, 1882–1884 (2003).

Acknowledgements

This research was supported by grants from the Korea Research Institute of Bioscience and Biotechnology (KRIBB) Research Initiative Program and R&D Convergence Program of the National Research Council of Science and Technology (NST) of Korea (CAP-14-3-KRIS). In addition, the National Research Foundation (NRF) of Korea supported this project (2016R1D1A1B03935393 and 2018R1A2B6008094).

Author Contributions

A.T. and S.K. initiated and directed the project, designed experiments, performed the experiments, carried out the theoretical modelling and calculations, analysed data and wrote the first version of the paper. Y.S., H.C., S.B. and J.S. performed the experiments and revised the paper. T.H.H. and S.H.P. initiated and supervised the project.

Additional Information

Supplementary information accompanies this paper at <https://doi.org/10.1038/s41598-019-38699-0>.

Competing Interests: The authors declare no competing interests.

Publisher's note: Springer Nature remains neutral with regard to jurisdictional claims in published maps and institutional affiliations.



Open Access This article is licensed under a Creative Commons Attribution 4.0 International License, which permits use, sharing, adaptation, distribution and reproduction in any medium or format, as long as you give appropriate credit to the original author(s) and the source, provide a link to the Creative Commons license, and indicate if changes were made. The images or other third party material in this article are included in the article's Creative Commons license, unless indicated otherwise in a credit line to the material. If material is not included in the article's Creative Commons license and your intended use is not permitted by statutory regulation or exceeds the permitted use, you will need to obtain permission directly from the copyright holder. To view a copy of this license, visit <http://creativecommons.org/licenses/by/4.0/>.

© The Author(s) 2019